# Can changes in deformation regimes be inferred from crystallographic preferred orientations in polar ice?

Maria-Gema Llorens[1*], Albert Griera[2], Paul D. Bons[3,4], Ilka Weikusat[3,5], David J. Prior[6], Enrique Gomez-Rivas[7], Tamara de Riese[3], Ivone Jimenez-Munt[1], Daniel García-Castellanos[1] and Ricardo A. Lebensohn[8]

[1] Geosciencies Barcelona CSIC, Lluis Sole i Sabaris s/n, 08028 Barcelona, Spain

[2] Departament de Geologia, Universitat Autònoma de Barcelona, 08193 Cerdanyola del Vallès, Barcelona, Spain

[3] Department of Geosciences, Eberhard Karls University Tübingen, Wilhemstr. 56, 72074 Tübingen, Germany

[4] China University of Geosciences, Beijing, China

[5] Alfred Wegener Institute Helmholtz Centre for Polar and Marine Research, Germany

[6] Department of Geology, University of Otago, 362 Leith Street, Dunedin 9016. New Zealand

[7] Departament de Mineralogia, Petrologia i Geologia Aplicada, Facultat de Ciències de la Terra, Universitat de Barcelona, Martí i Franquès s/n, 08028 Barcelona, Spain

[8] Theoretical Division. Los Alamos National Laboratory. Los Alamos, NM, 87545, USA

[*]*Corresponding author:* mgllorens@geo3bcn.csic.es (Maria-Gema Llorens)

***Keywords:*** *ice microstructures, crystallographic preferred orientation, ice-sheet flow, finite strain, flow transitions*

**Abstract**

Creep due to ice flow is generally thought to be the main cause for the formation of crystallographic preferred orientations (CPOs) in polycrystalline anisotropic ice. However, linking the development of CPOs to the ice flow history requires a proper understanding of the ice aggregate's microstructural response to flow transitions. In this contribution the influence of ice deformation history on the CPO development is investigated by means of full-field numerical simulations at the microscale. We simulate the CPO evolution of polycrystalline ice under combinations of two consecutive deformation events up to high strain, using the code VPFFT/ELLE. A volume of ice is first deformed under co-axial

boundary conditions, which results in a CPO. The sample is then subjected to different
boundary conditions (co-axial or non-coaxial) in order to observe how the deformation
regime switch impacts the CPO. The model results indicate that the second flow event tends
to destroy the first, inherited fabric, with a range of transitional fabrics. However, the
transition is slow when crystallographic axes are critically oriented with respect to the second
imposed regime. Therefore, interpretations of past deformation events from observed CPOs
must be carried out with caution, particularly, in areas with complex deformation histories.

## 1. Introduction

During the last two decades sea level rise has accelerated in association with global climate
change (Nerem et al., 2018), but the limited knowledge available on how fast ice flows in ice
sheets along with uncertain boundary conditions (Edwards et al., 2021) give a wide range in
long-term sea level rise predictions. The rheological changes of polar ice during its
deformation are crucial for the accurate projection of ice sheet discharge into the ocean
(Golledge et al., 2015). Polycrystalline ice (ice *1h*) in glaciers, ice sheets and ice shelves
flows in response to gravitational forces (e.g., Hudleston, 2015). Crystal-plastic strain of ice
is mainly accommodated by the glide of dislocations along their individual crystallographic
slip systems (Duval, 1983). Deformation of a grain aggregate by dislocation creep leads to a
crystallographic preferred orientation (CPO), also called fabric or texture. The CPO evolves
according to the flow kinematics, magnitude of strain and temperature (Budd and Jacka,
1989; Katayama and Karato, 2006; Qi et al., 2019; Fan et al., 2020), and importantly depends
on the activity of, or ease of glide of dislocations on the different slips systems. An ice crystal
is strongly anisotropic because it deforms predominantly by the glide of dislocations on the
basal plane (0001) and along the *a*-axes <11-20> direction (Duval et al., 1983). The gravity-
driven flow of ice sheets produces rotations of ice crystal lattices, developing CPOs
according to the stress configuration (Treverrow et al., 2012). The *c*-axes (normal to the basal
plane) tend to get oriented in a cone-shaped distribution of *c*-axes with the cone axis parallel
to the maximum compressional finite strain (Qi et al., 2017). *a*-axes tend to be parallel to the
maximum extensional finite strain at low temperature and high strain (Qi et al., 2019;
Journaux et al., 2019), while they present a tendency to become parallel to the vorticity axis
at high temperature (Qi et al., 2019), also according to CPO descriptions of ice natural
samples (Monz et al., 2021; Thomas et al., 2021) For that reason, the observed CPO in ice
cores drilled in ice sheets and glaciers is assumed as a reliable macroscopic flow indicator

(Hudleston, 1977; Alley, 1988). Microstructures described from ice cores drilled in Antarctica and Greenland have allowed the interpretation of deformation conditions (see table 1 in Faria et al., 2014). However, because ice can be affected by differences in temperature and stress configurations during ice-sheet flow, unravelling the ice deformation history from $c$-axis fabrics observed in natural ice samples can be challenging. The fact that most deep ice cores are drilled at ice-sheet divides or domes, with the aim of providing the best-quality paleoclimate record, does not help in gaining understanding of natural ice flow from the recovered ice samples.

Most of the current knowledge of the link between ice deformation and CPO development is derived from laboratory experiments. Experimental studies have utilised ice to understand how CPOs develop and evolve under deformation (Kamb et al., 1972; Wilson, 1982; Jacka and Maccagnan, 1984, Wilson and Peternell, 2012; Budd et al., 2013; Montagnat et al., 2015; Vaughan et al., 2017, Fan et al., 2020). Most studies by far use bulk isotropic ice (i.e., with a random CPO) that is then subjected to a single deformation event. Due to the limitations of laboratory deformation experiments, to our knowledge only a few studies have used polar ice samples starting with a pre-existing CPO. Moreover, most of such studies focused on vertical uniaxial compression of samples with a pre-existing CPO that was formed by vertical compression (resulting in a $c$-axis cluster or cone) (Azuma and Higashi, 1984; Dahl-Jensen et al., 1997, Castelnau et al., 1998, Jacka and Li, 2000, Fan et al., 2020). Exceptions are the experiments by Jun and Jacka (1998) and Treverrow et al. (2012), in which the compressional CPO is deformed under horizontal shear, and Craw et al. (2018), where vertical axial compression is applied to sub-samples taken at different angles from a sample with a pre-existing vertical girdle orientation. Numerical modelling provides an alternative approach to overcome these limitations because it allows a continuous analysis of multiple deformation scenarios with a wide variety of deformation kinematics and environmental parameters. Moreover, numerical simulations of polycrystalline ice and their comparison with experimental and natural data provide useful insights into the study of the CPO development, as they allow visualizing and quantifying the microstructural evolution up to high strain (Montagnat et al., 2014b; Piazolo et al., 2019). However, as in the case of laboratory experiments, most numerical studies to date have focused on systems starting with an initially random CPO to which a single deformation event is applied (Montagnat et al., 2011; Llorens et al., 2017, 2020). Although very useful, these experimental and numerical studies can only represent a limited range of real natural scenarios, where ice aggregates with no strain history

are subjected to stress. To date only a few modelling studies have addressed the issue of the evolution of polycrystalline ice that has previously experienced flow. Examples are Thorsteinsson et al. (2003), which evaluates to what extent an observed CPO tracks the local stress within an ice sheet, and Jansen et al. (2016), where the viscoplastic response of ice polycrystals with a starting CPO is studied. More recently, Lilien et al. (2021) analyse whether the effect of changes in ice-stream flow can be recorded in ice-crystal fabrics.

Considering that volumes of polar ice typically experience multiple changes in the deformation regime along their flow path during ice-sheet flow, such as the transition from the co-axial strain in the centre of the ice mass to non-coaxial strain at depth and away from the centre (Jennings and Hambrey, 2021), systematic studies providing a comprehensive understanding of CPO development during multi-stage deformation histories are essential. Hence, this contribution intends to fill this knowledge gap by providing a study of the multi-stage deformation of ice samples and the resulting CPOs for different settings. We present a series of numerical simulations of polycrystalline ice that is affected by two consecutive deformation events. We choose combinations of subsequent deformation kinematics that may be expected to occur in ice sheets. We analyse the CPO developed during these deformation events in order to determine the kinematic conditions for the preservation, modification or destruction of CPOs in ice.

## 2. Flow regime transitions in polar ice sheets

Ice flows in all directions from the accumulation zone towards the edges of the ice mass driven by the gravity force. Due to precipitation and accumulation, ice is gradually compressed ranging from vertical axial compression in domes, to plane strain vertical compression in ridges (zone I in Fig. 1a). Observations from natural ice core samples at these domains range from a vertical single maximum to a vertical girdle (Montagnat et al., 2012; Weikusat et al., 2017). At depth and away from the centre of the ice sheet (zone II in Fig. 1a), ice experiences a vertical gradient in velocity, resulting in simple shear deformation parallel to the bedrock (Hudleston, 2015). At depth, observations from ice cores indicate a vertical single maximum. Inside a glacier, ice stream or in a flank flow (Voigt, 2017) flow acceleration may dominate, resulting in extension along the flow direction (zone III in Fig. 1a), observed by a vertical girdle in ice core samples (Voigt, 2017). In a shear margin of glaciers and ice streams, as well as in some ice shelves, ice experiences a gradient in velocity

in the lateral direction perpendicular to that velocity, resulting in simple shear deformation with a vertical shear plane (zone III and IVa in Fig.1a-b), observed by a single or double maxima (Jackson and Kamb, 1997) oriented sub perpendicular to the shear plane (Monz et al., 2021; Thomas et al., 2021) and consistent with geophysical data (Smith et al., 217; Lutz et al., 2020, 2022).

In this contribution, we analyse different examples of flow changes that represent relevant and/or common deformation regimes in ice sheets (zones I to IV in Figure 1), assuming a constant strain rate and temperature.
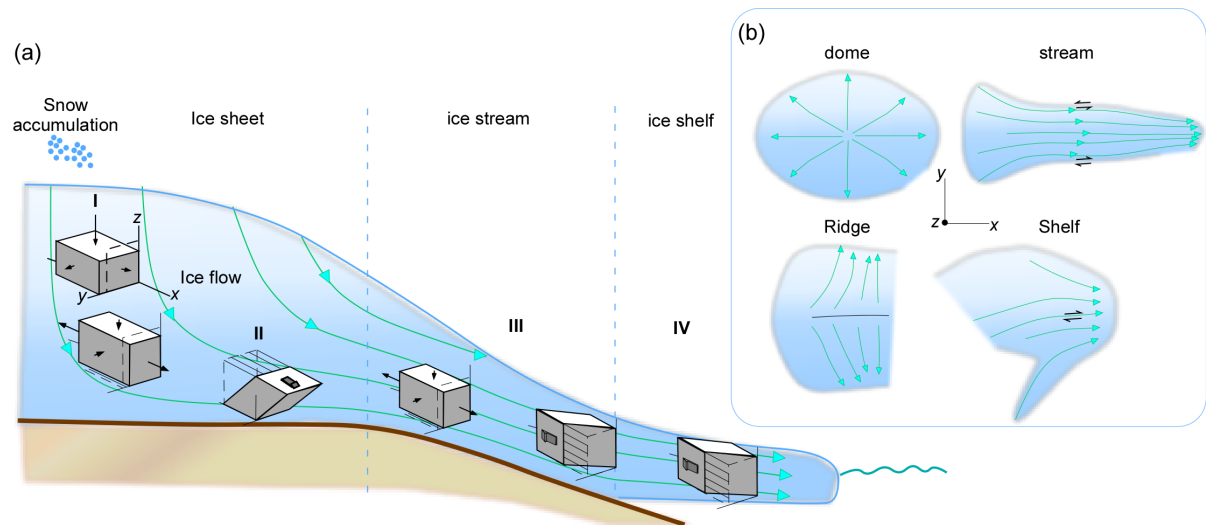
**Figure 1.** Sketch of ice-sheet flow patterns in (a) cross section and (b) map view, showing some dominant deformation conditions at different zones of the ice mass. At the upper and central parts of the dome the dominant flow regime is vertical axial compression parallel to $z$ (indicated by zone I). In ice ridges, an extension flow transverse to the ridge can occur (Wang et al., 2002). Flow turns progressively more non-coaxial with depth and distance from the dome, where strongly non-coaxial deformation dominates close to the bedrock (indicated by zone II). The dominant kinematic regime at the ice stream is extension along the flow direction, where simple shear deformation with a vertical shear plane can occur in shear margins of the stream (indicated by zone III). At the ice shelf, the predominant regime assumed in this contribution is simple shear in the horizontal plane ($xy$) (zone IV) (Lutz et al., 2020). The $xyz$ reference frame is defined with $z$ vertical, $x$ horizontal and parallel to flow and $y$ normal to $xz$:

## 3. Methods

### 3.1. Numerical simulation of ice fabrics and postprocessing

Ice polycrystalline viscoplastic deformation was simulated using the Fast Fourier Transform

algorithm (VPFFT; Lebensohn and Rollett, 2020), within the numerical open-source platform ELLE (http://www.elle.ws; Bons et al., 2008). The coupling of the full-field VPFTT code and ELLE allows simulating deformation of a polycrystalline aggregate by dislocation glide up to high strains (>10) as often found in nature in ice and rocks. The reader is referred to Lebensohn and Rollett (2020) for a detailed description of the VPFFT approach, and to Griera et al. (2013) and Llorens et al. (2016a) for a detailed description of the coupling between VPFFT and ELLE. The local mechanical response of a nonlinear heterogeneous material can be calculated as a convolution integral of the Green functions associated with a linear homogenous medium and a polarisation field. The VPFFT formulation is used to transform the polarisation field that contains all the information on the heterogeneity and non-linearity of the material's behaviour into Fourier space. By the conversion of the real space convolution integrals to simple products in the Fourier space, the mechanical fields are calculated, and the convolution product is transformed back to real space. In this full-field approach, the semi two-dimensional data structure is discretised by a regular mesh of 256x256 unconnected nodes (*unodes*) or Fourier points (Fig. 2b). The strain rate and stress field under compatibility and equilibrium constraints related by the constitutive equation (1) is obtained by iteratively solving for the flow law for every *unode* (*u*):

$$\dot{\varepsilon}_{ij}(u) = \sum_{s=1}^{N} m_{ij}^{s}(u)\dot{\gamma}^{s}(u) = \dot{\gamma}_0 \sum_{s=1}^{N} m_{ij}^{s}(u) \left( \frac{\left| m_{ij}^{s}(u)\sigma_{ij}'(u) \right|}{\tau^{s}(u)} \right)^{n} \times \text{sgn}\left( m_{ij}^{s}(u)\sigma_{ij}'(u) \right)$$

(1)

Where $\dot{\varepsilon}_{ij}$ is the strain rate, $\sigma_{ij}'$ is the deviatoric stress, $m_{ij}^{s}$ is the symmetric Schmid tensor, $\dot{\gamma}^{s}$ the shear strain rate, $\tau^{s}$ is the critical resolved shear stress defined for the slip system (*s*) , $\dot{\gamma}_0$ is a reference strain rate and *n* is the stress exponent.

In all three slip systems, the shear strain rate is assumed to be related to the deviatoric stress by a stress exponent of *n*=3, in accordance with the "Glen's law" (Haefeli,1961). After convergence, the VPFFT code calculates the associated lattice rotations from the velocity gradient and stress fields. The actual stress exponent in ice 1h may actually be closer to *n*=4 (Bons et al., 2018; Qi and Goldsby, 2021). The first tests show that raising *n* to 4 has little effect on the CPO, and in order to be coherent with previous ice CPO simulations (Llorens et al., 2016a, 2016b, Steinbach et al., 2016, Jansen et al., 2016; Qi et al., 2019; Piazolo et al.,

2019) all simulations presented here are carried out with the more commonly used $n=3$.

Uniaxial shortening of a single crystal by glide only along the non-basal planes requires about 60 times higher stress than when the crystal can deform entirely by basal-plane glide (Duval et al., 1983). We therefore set $\tau^s$ 60 times lower for basal glide than for prismatic and pyramidal glide.

Previous numerical studies have shown that about the same single-maximum CPO develops at low temperature and a high strain rate conditions, regardless of the set rate of dynamic recrystallisation (see supplementary figure 4 or Llorens et al., 2016a; 2016b). As this contribution aims to study the CPO response to a change in the deformation regime, the numerical procedures that simulate dynamic recrystallisation (Llorens et al., 2017) are deliberately not incorporated. Every *unode* represents a *crystallite* where the crystal orientation, strain rate, dislocation density and local stress is stored (Fig.2b). All *unodes* inside a grain have the same initial crystal orientation (Fig.2a). The crystal orientation is defined by the three Euler angles. We use the three Euler angles stored at every *unode* of the model for the calculation of the orientation density function (ODF) that provides the orientation densities in Euler space, using the open-source texture analysis software MTEX (Bachmann et al., 2011). The intensity of the CPO is shown by the misorientation index (M-index; Skemer et al., 2005) calculated from the ODF. Crystal symmetry shows the relative proportion of point (P), girdle (G) and random (R) components of the (0001) crystallographic axis, or *c*-axis distribution in a ternary diagram (Vollmer, 1990). The P, G and R proportion is calculated from the three eigenvalues ($a_1$, $a_2$, $a_3$) as P=$a_1 - a_2$, G=$2a_2 - a_3$ and R=$3a_3$.
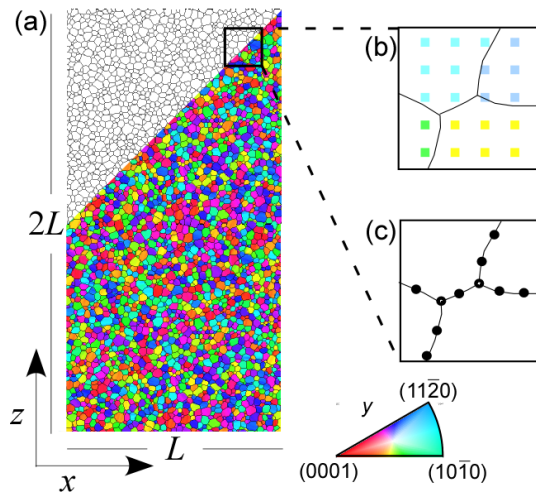
**Figure 2**. (a) The initial microstructure is a 2 x 1 model unit length (*L*). Two data layers are used in the ELLE approach: (b) the microstructure is discretised by a mesh of 256x256

*unodes* or Fourier points. (c)The boundary nodes (*bnodes*) layer defines grains.

220

## 3.2. Simulated flow regimes and applied boundary conditions

Deformation was applied to the microstructure by incremental steps of a shear strain of $\gamma=0.04$ or, alternatively, 2% of shortening or extension (Table 1), both equivalent to 0.02

225     natural strain, defined as $\ln(L_f/L_i)$ (with $L_f$ and $L_i$ being the final and initial length of a line in the direction of maximum extension, respectively). Each example considered in this contribution consists of two deformation regimes that are applied in succession (see Table 2 and supplementary figure 5). We considered four different model series (series A to D) to simulate flow transitions between pairs of deformation regimes (**V**) that dominate in different

230     zones of the ice mass through which a volume of ice may travel.
Series A represents ice flowing from the centre of a dome to deep lateral zones (from zone I to zone II in Fig. 1). To simulate this transition, we carried out a series of simulations with first vertical uniaxial compression parallel to $z$ (**V$_1$**), followed by top-to-the-right simple shear in the vertical plane (*xz*) with a horizontal shear plane (**V$_2$**) (Table 1 and 2). Similar to A,

235     Series B shows the transition of ice flowing in central parts of the ice sheet, but in this case from the centre of a ridge to deep lateral zones (from zone I to zone II in Fig. 1). For series B, we considered that the ice aggregate is first deformed by **V$_3$**, horizontal uniaxial extension parallel to $x$, followed by **V$_2$**, dextral simple shear in the vertical plane (*xz*) as in Series A (Table 1 and 2). Series C simulates ice flowing from an ice dome to an ice flank or stream

240     (from zone I to zone III in Figure 1). Series C was carried out assuming first vertical uniaxial compression parallel to $z$ (**V$_1$**) followed by uniaxial extension parallel to $x$ (**V$_3$**) (Table 1 and 2). Finally, series D represents ice flowing from an ice-stream or glacier to an ice shelf or shear margin (from zone III to zone IV in Figure 1). For this series, we considered first uniaxial extension in the $x$ direction (**V$_3$**), and subsequent dextral simple shear in the

245     horizontal plane (*xy*) with a vertical shear plane parallel to the flow direction (**V$_4$**) (Table 1 and 2). As a ridge can be represented by confined compression and extension, rather than pure extension, a sensitivity test of series B, C and D assuming pure shear (**V'$_3$**) (Table 1) can be found in supplementary figures 1, 2 and 3. For comparison, results from simulations of microstructures deformed under a single-deformation event (**V$_2$**, **V$_3$** and **V$_4$**) are shown

250     together with all series results.

**Table 1**. Velocity gradient tensors **V** considered for the different regimes and corresponding zones in Figure 1.

The *xyz* reference frame is defined with *z* vertical, *x* horizontal and parallel to flow and *y* normal to *xz*.

| Name | Regime | Zone (Figure 1) | Velocity gradient tensor |
|---|---|---|---|
| $V_1$ | Vertical uniaxial compression parallel to *z*, extension in *x* and *y* | I | $\begin{bmatrix} 0.01 & 0 & 0 \\ 0 & -0.02 & 0 \\ 0 & 0 & 0.01 \end{bmatrix}$ |
| $V_2$ | Dextral simple shear in the vertical plane (*xz*), plane strain | II | $\begin{bmatrix} 0 & 0.04 & 0 \\ 0 & 0 & 0 \\ 0 & 0 & 0 \end{bmatrix}$ |
| $V_3$ | Horizontal uniaxial extension parallel to *x*, compression in *y* and *z* | I, III | $\begin{bmatrix} 0.02 & 0 & 0 \\ 0 & -0.01 & 0 \\ 0 & 0 & -0.01 \end{bmatrix}$ |
| $V'_3$ | Pure shear, plane strain | I, III | $\begin{bmatrix} 0.02 & 0 & 0 \\ 0 & 0.02 & 0 \\ 0 & 0 & 0 \end{bmatrix}$ |
| $V_4$ | Dextral simple shear in the horizontal plane (*xy*), plane strain | III, IV | $\begin{bmatrix} 0 & 0 & -0.04 \\ 0 & 0 & 0 \\ 0 & 0 & 0 \end{bmatrix}$ |

**Table 2**. Deformation regimes applied to the different series of numerical simulations, including idealised deformation regimes in drill cores and examples. References of ice core description: GRIP (Thorsteinsson et al., 1997), GISP2 (Gow et al., 1997), Dome C (Durand et al., 2007), Dome F (Azuma et al., 1999), Talos Dome (Montagnat et al., 2012), NorthGRIP (Faria et al., 2014); EDML (Weikusat et al., 2017), NEEM (Montagnat et al., 2014a), Vostok (Lipenkov et al., 1998)

| Name | First + Second regime | Application of the second regime | Ice core | Drill core regime |
|---|---|---|---|---|
| Series A | $V_1 + V_2$ | At the last step ($\varepsilon_I$=0.92) | GRIP, GISP2, Dome C, Dome F, Talos Dome | Dome/Summit |
| Series B | $V_3 + V_2$ | At the last step ($\varepsilon_I$=0.92) | NorthGRIP, EDML, NEEM | Divide |
| Series C | $V_1 + V_3$ | At steps of $\varepsilon_I$ = 0, 0.2, 0.4, 0.8 and 1.2 | Spice, Vostok | Flank flow |
| Series D | $V_3 + V_4$ | At the last step ($\varepsilon_I$=0.92) | | Shear margin |

## 4. CPO evolution results

### 4.1. Series A: Ice flowing from the centre of the dome to deep lateral zones

265 Snow precipitation at a dome causes vertical uniaxial compression and flattening of ice layers, and outflow in all horizontal directions (zone I in Fig. 1). As ice flows away from domes and gets buried deeply it enters the zone dominated by simple shear parallel to the bedrock (zone II in Fig. 1). To simulate this transition, the initial randomly oriented microstructure in series A is first subjected to vertical uniaxial compression parallel to $z$ ($V_1$), followed by dextral

270 simple shear in the vertical plane ($xz$) ($V_2$) (Table 1 and 2). The pole figures in Figure 3 show the crystallographic preferred orientation evolution during deformation in Series A. The initially untextured microstructure (*i.e.*, with an initially homogeneous and random lattice orientation, see Fig. 3a) develops a strong CPO due to the rotation of $c$-axes towards the maximum shortening direction, according to the imposed vertical compression (see Fig.3a at

275 $\varepsilon_1$=0.92). The observed CPO symmetry, expressed as the proportion of point (P), girdle (G) and random (R) components of $c$-axes (0001), is characterised by a point maximum with no girdle component (Fig. 3c). The final step of the first regime ($\varepsilon_1$=0.92) is used as the initial texture for the second deformation regime simulation, where the aggregate is subjected to simple shear in the vertical plane ($xz$) up to a total natural strain of 4 (see $\varepsilon_2$=3 Fig. 3b).

280
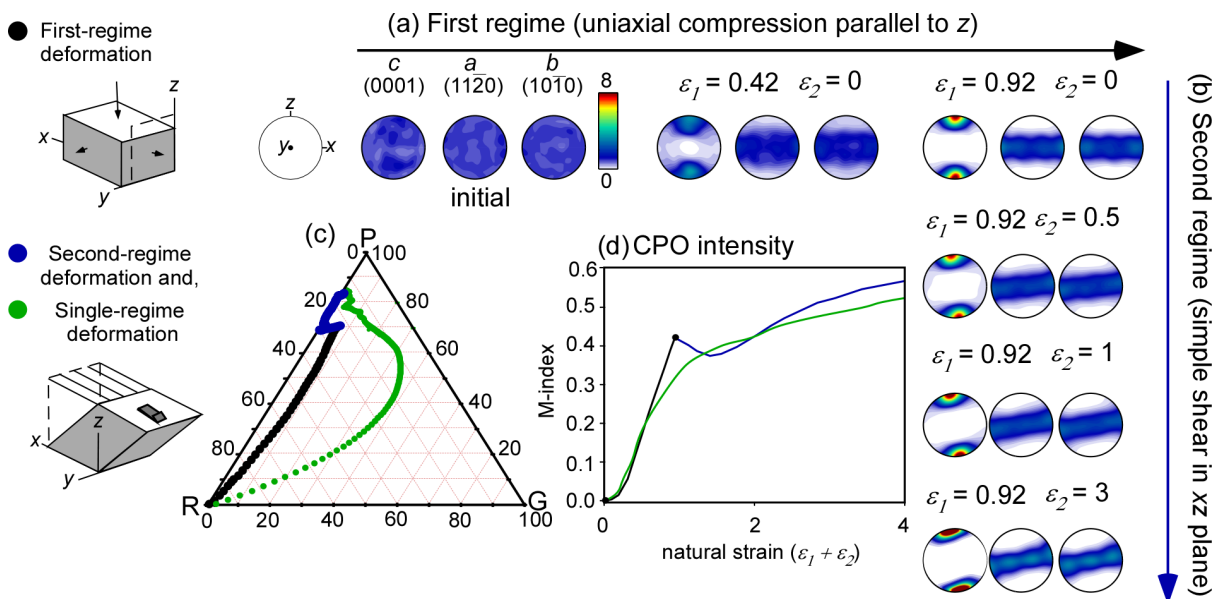
**Figure 3.** CPO evolution during the two consecutive deformation regimes of series A: (a) vertical uniaxial compression parallel to $z$ (black) and subsequently (b) dextral simple shear in the vertical plane $xz$ (blue). The

final texture developed at the end of the first flow regime is used as the initial texture (input) for simulating the second regime. (c) Ternary diagram that shows the CPO symmetry expressed as the proportion of point (P), girdle (G) and random (R) components of $c$-axes (0001). Points plotted at the PGR graph represent every step of deformation ($\varepsilon = 0.02$). (d) The CPO intensity is quantified as the M-index from the ODF (misorientation index, Skemer et al., 2005) and its evolution with cumulative strain so shown. The evolution of the CPO in simple shear only, starting with a random fabric (single-regime deformation), is shown in green in both (c) and (d).

At the beginning of the second regime the CPO slightly rotates antithetically (*i.e.*, opposite to the imposed shear sense) (see $\varepsilon_2=1$ in Fig. 3b), while the CPO intensity (Fig. 3d) and girdle component decrease (Fig. 3c). After that the CPO intensity (point maximum) gradually intensifies again and the $c$-axes align at about 10° to the normal to the shear plane (see $\varepsilon_2=3$ in Fig. 3b and Fig. 3c). After the two deformation events the resulting CPO resembles the one resulting from simple shear deformation only, in both CPO intensity and symmetry (green and blue markers in Fig. 3d and Fig. 3c). This implies that the previous uniaxial flattening regime is not recognizable after only a moderate amount ($\varepsilon_1>1$) of subsequent simple shear, as may be expected as the change in CPO only involves a small rotation and intensification of the $c$-axes point maximum.

### 4.2. Series B: Ice flowing from the centre of the ridge to deep lateral zones

On ridges away from ice domes, ice flows away and stretches in the direction perpendicular to the ridge (Wang et al., 2002; Faria et al., 2014) (zone I in Fig. 1). Here we consider the end-member case that this leads to uniaxial extension in the flow direction. Similar to Series A, the ice is then assumed to be buried and to enter zone II (Fig. 1) where flow is dominated by bedrock-parallel simple shear, again in the direction perpendicular to the ridge (zone II in Fig. 1). For this case, the initial microstructure is first deformed by $\mathbf{V_3}$, horizontal uniaxial extension parallel to $x$, followed by $\mathbf{V_2}$, dextral simple shear in the vertical plane ($xz$) (Table 1 and 2). A sensitivity test of series B, where the first deformation regime applied is pure shear ($\mathbf{V'_3}$ in table 1) is shown in supplementary figure 1.

In series B, the initially random distributed $c$-axes develop a CPO characterised by a strong vertical girdle, in coherence with the horizontal extension applied during the first deformation regime (see $\varepsilon_1=0.92$ in Fig. 4a). From the final step onwards, the aggregate is deformed under simple shear in the vertical plane ($xz$) up to a natural strain of $\varepsilon_2=4$ (Fig. 4b). $C$-axes reorient following the new flow, destroying the vertical girdle fabric (Fig. 4c), and forming a broad

single point maximum almost normal to the shear plane (see $\varepsilon_2=4$ in Fig. 4b). Although the final CPO symmetry is coherent with simple shear deformation, its shape after a strain of

320    $\varepsilon_2=4$ still differs from that of the previous case (series A) or that of simple shear only (see the last step for the second regime in Figs. 3a and 4a). At the highest modelled strain ($\varepsilon_2=4$) the CPO intensity is clearly lower than that developed under solely simple shear deformation (Fig. 4d). Changing a girdle to point maximum requires a significantly higher strain than the formation of a point maximum only (green versus blue graph in Fig.4d).

325
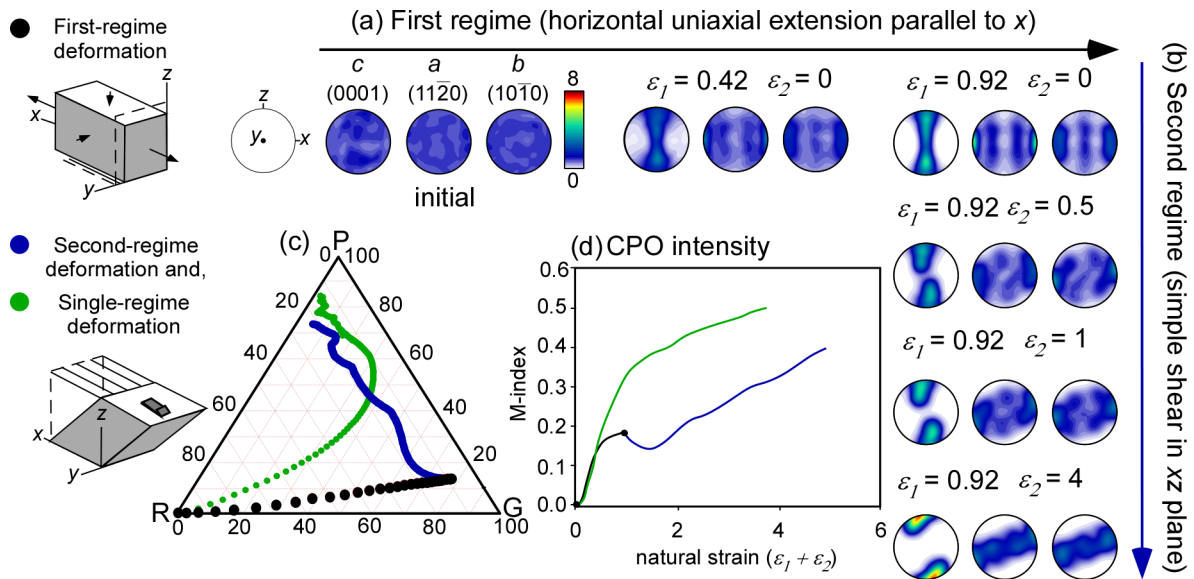
**Figure 4.** CPO evolution during the two consecutive deformation regimes of series B. The final texture at the end of the first flow regime (a), is used as initial texture for the second regime (b). (c) Ternary diagram that shows the CPO symmetry expressed as the proportion of point (P), girdle (G) and random (R) components of $c$-

330    axes (0001). Points plotted at the PGR graph represent every step of deformation ($\varepsilon = 0.02$). (d) The CPO intensity is quantified as the M-index from the ODF. The evolution of the CPO in simple shear only, starting with a random fabric (single-regime deformation), is shown in green in both (c) and (d).

## 4.3. Series C: Ice flowing from an ice dome to an ice flank or stream

335

In this configuration we assume that ice is first gradually flattened by vertical uniaxial compression parallel to $z$ in an ice dome (**V$_1$**; zone I in Fig. 1) and subsequently enters a zone in which the flow accelerates in, for example, an ice stream, leading to uniaxial extension in the flow direction (**V$_3$**; zone III in Fig. 1). Series C includes a set of simulations where **V$_3$**

340    deformation starts at different strains in the first stage with **V$_1$**. A sensitivity test of series C, where the second deformation regime applied is pure shear (**V'$_3$** in table 1) is shown in

supplementary figure 2.

The microstructure in series C first develops a strong CPO (Fig. 5b) with a point maximum in the $z$-direction of the axial compression applied during the first deformation regime (see first row in Fig. 5a). In this series the second deformation regime was applied at different steps of natural strain of the first regime (at $\varepsilon_1$=0.2, 0.4, 0.8 and 1.2, respectively). The intensity of the initial deformation regime has a notable influence on the CPO developed during the second regime. In the absence of first-regime deformation ($\varepsilon_1$=0.0), where the microstructure only experiences uniaxial extension in the $x$-direction, a vertical girdle fabric develops (see first column in Fig. 5a and green marker Fig. 5b). Regardless of the step at which the second regime is applied, the CPO tends to evolve towards a girdle fabric (see evolution of all series in Fig. 5a-b), which slightly reduces the CPO intensity of the start of the second regime (Fig. 5c). If the second deformation regime is applied when the microstructure has only been slightly affected by the first regime ($\varepsilon_1 < 0.4$), the $c$-axes tend to rotate forming a final girdle fabric but with a recognizable point maximum component, resulting in an "hourglass shape" (see second and third columns in Fig. 5a). However, if a strong point maximum CPO developed during the first deformation regime ($\varepsilon_1 > 0.8$), the second regime cannot modify the inherited $c$-axis orientation at a natural strain of $\varepsilon_2 = 1.2$ (see fifth column in Fig. 5a), and the final CPO continues being dominated by a strong point maximum (Fig. 5b). The effect of the second regime is observable in the $a$-axis distribution, because regardless of the intensity of the first regime, the extension along the x direction produces three $a$-axis maxima (see last row in Fig. 5a). The result suggests that converting a point maximum into a girdle takes even more strain than the opposite (Series B).
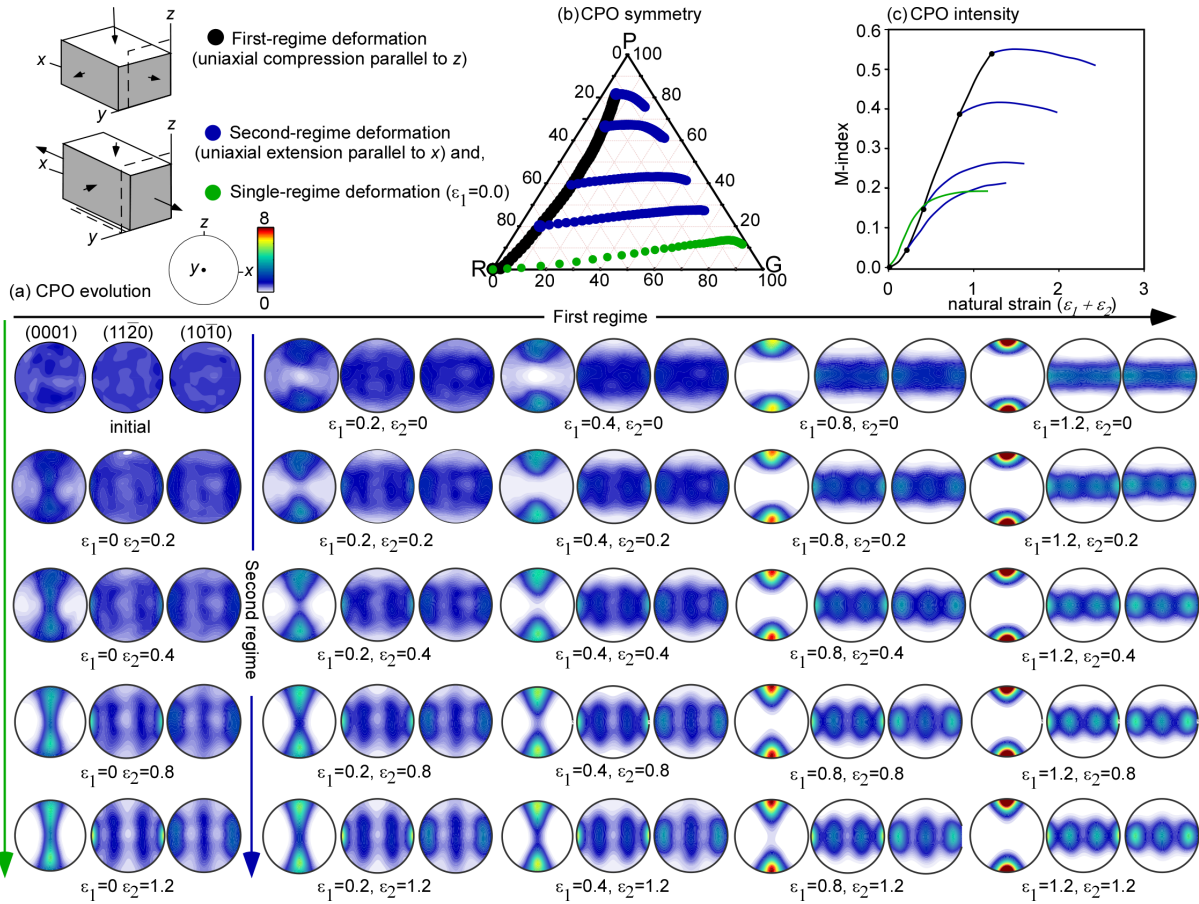
**Figure 5.** (a) CPO evolution during two consecutive deformation regimes of series C. Textures developed at different steps of natural strain in the first regime ($\varepsilon_1$) are used as initial textures for the second regime ($\varepsilon_2$). (b) Ternary diagram that shows the CPO symmetry expressed as the proportion of point (P), girdle (G) and random (R) components of $c$-axes (0001). (c) The CPO intensity is quantified as the M-index from the ODF. The evolution of the CPO in uniaxial extension parallel to $x$ only, starting with a random fabric ($\varepsilon_1$=0: single-regime deformation), is shown in green in both (b) and (c).

## 4.4. Series D: Ice flowing from an ice-stream or glacier to an ice shelf or shear margin

Dominantly simple shear deformation in the horizontal plane takes place in the margins of ice streams (Hudleston, 2015) and can be found in some ice shelves (Young et al., 2002; LeDoux et al., 2017; Lutz et al., 2020) (zone IV in Fig.1). Ice affected by this shearing may have experienced different deformation types before. Here we consider the case of uniaxial extension in the flow direction (zone III in Fig.1), which would represent the ice above the deepest layers that thus did not experience bedrock-parallel simple shear. This series include a first deformation regime of uniaxial extension in the $x$ direction ($\mathbf{V_3}$), and subsequently dextral simple shear in the horizontal plane ($xy$) ($\mathbf{V_4}$). A sensitivity test of series D, where the first deformation regime applied is pure shear ($\mathbf{V'_3}$ in table 1) is shown in supplementary

figure 3.

In series D a vertical girdle fabric develops during the first deformation regime ($\varepsilon_1 = 0.92$ in Fig. 6a), which then rapidly evolves towards a point maximum due to simple shear in the horizontal plane ($xy$) imposed during the second flow regime (Fig. 6b). However, after significant strain there is still a girdle component.
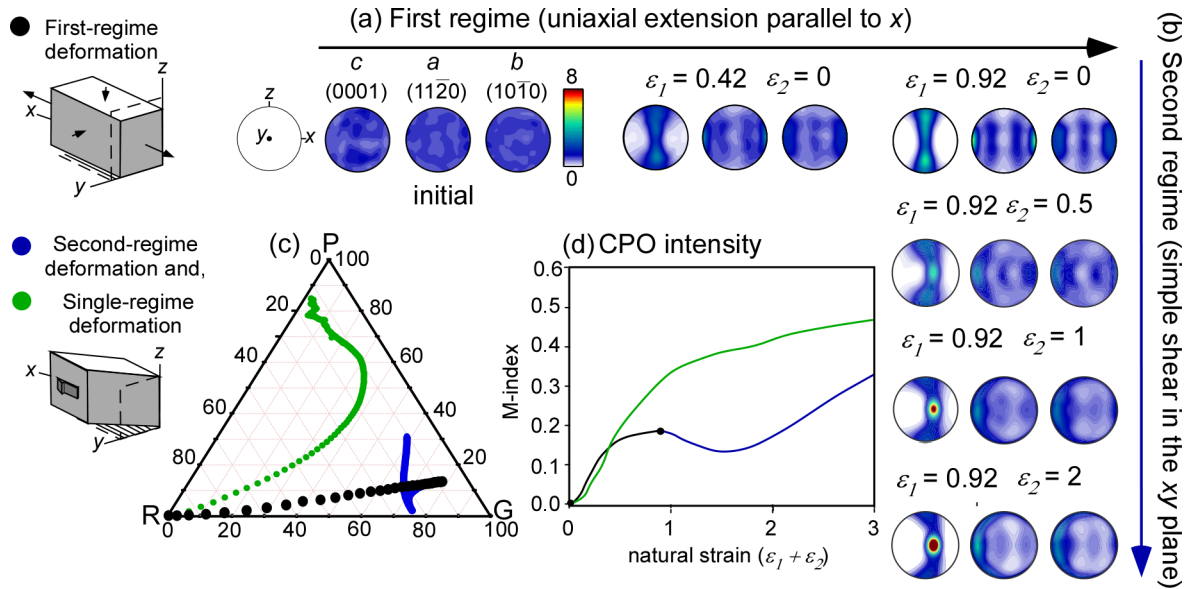
**Figure 6.** CPO evolution during the two consecutive deformation regimes of series D. The final texture at the end of the first regime (a), is used as initial texture for the second regime (b). (c) Ternary diagram that shows the CPO symmetry expressed as the proportion of point (P), girdle (G) and random (R) components of $c$-axes (0001). Points plotted at the PGR graph represent every step of deformation ($\varepsilon$=0.02). (d) The CPO intensity is quantified as the M-index from the ODF. The evolution of the CPO in simple shear only (single-regime deformation), starting with a random fabric, is shown in green in both (c) and (d).

## 5. Discussion

Experiments and simulations with an initial random distribution of crystallographic orientations predict a quick alignment of the crystallographic axes according to the imposed deformation conditions (Azuma and Higashi, 1984; Qi et al., 2019, Llorens et al., 2016a; Llorens et al., 2016b; Peternell and Wilson, 2016; Wilson et al., 2020). The types and orientations of CPOs are best described in terms of the principal axes of the finite-strain ellipsoid (FSE), also known as finite stretching axes (FSA's) that are typically labelled $X$, $Y$ and $Z$ from longest to shortest (Fig.7) (Passchier, 1990). These axes are parallel to the instantaneous stretching axes (ISA's) in the case of coaxial deformation, but not in the case of simple shear. In simulations, $c$-axes tend to align themselves parallel to the shortening FSA's.

In the case of uniaxial compression ($\mathbf{V_1}$ in Table 1; *X=Y>Z*) this leads to the development of a strong point maximum. The development of a vertical single maximum observed in vertical uniaxial compression simulations performed (first-regime deformation in series A and C) match observations from Antarctic natural ice core samples, as the EPICA Dome C (Durand et al., 2007), Dome F (Azuma et al., 1999), Talos Dome (Montagnat et al., 2012), and Greenland ice cores GISP2 (Gow et al., 1997) and GRIP (Thorsteinsson et al., 1997). They also match laboratory experiments carried out at low temperatures and high strain rates (Craw et al., 2018; Fan et al., 2020). A girdle forms in uniaxial extension ($\mathbf{V_3}$ in Table 1; *X>Y=Z*). The vertical girdle fabric predicted in our simulations under uniaxial extension (first-regime deformation in series B and D) is also observed in Antarctic and Greenland ice cores, such as the Vostok ice core (Lipenkov et al., 1998; Voigt, 2017), EPICA DML (Weikusat et al., 2017), NEEM (Montagnat et al., 2014a) or in the Styx Glacier in Northern Victoria Land (Kim et al., 2020). As described in the NorthGRIP Greenland ice core, the vertical girdle is interpreted as evidence for extension transverse to the ridge, where the vertical girdle plane is oriented perpendicular to the axis of horizontal extension (Wang et al., 2002; Faria et al., 2014; Weikusat et al., 2017).

In simple shear ($\mathbf{V_2}$ and $\mathbf{V_4}$) the orientation of the *Z*-axis rotates from initially 45° to 0° to the shear plane at infinite strain, while the *X*-axis remains in the shear plane. A point-maximum CPO is expected and observed parallel to *Z* in the plane between the instantaneous shortening axis and the normal to the shear plane. *a*-axes (11-20) align themselves perpendicular to the *c*-axes in the plane of the two least compressive FSA's (*i.e.* the *X* and *Y*-axes of the finite-strain ellipsoid) (see first column in Fig. 7).
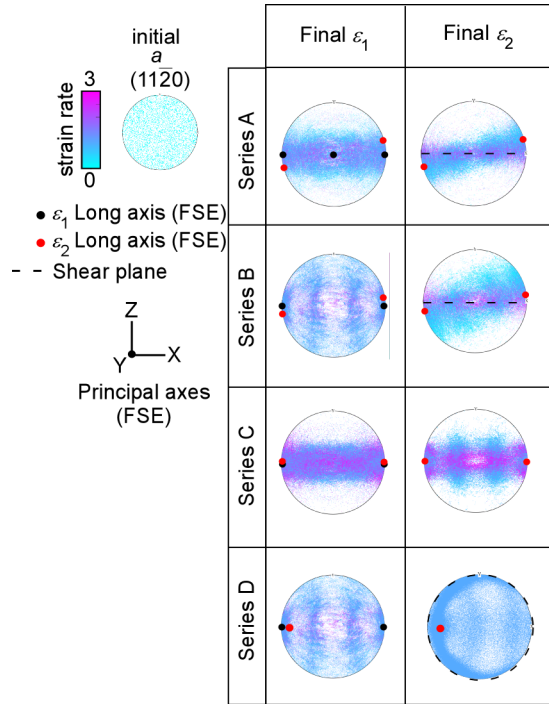
**Figure 7.** Pole figures of *a*-axis (11-20) orientation at the end of the first stage of deformation ($\varepsilon_1$) and the beginning and the end of the second stage of deformation ($\varepsilon_2$) for all series presented. The colour code in pole figures indicates the Von Mises strain rate normalised with respect to the bulk value per point (*unode*). The orientation of the elongation axis of the finite-strain ellipsoid (FSE) is indicated in solid black or red dots for the first and second stage of deformation, respectively. The shear plane in simple shear simulations is plotted as a black dashed line. When the maximum elongation axis lies within the *a*-axis girdle (series C and D), the inherited CPO is not completely overprinted at the end of the simulation.

440

The results from plausible scenarios studied here reveal that when a second deformation regime affects the microstructure the inherited CPO gets overprinted, and the CPO evolves according to the new kinematics of deformation. Regardless of the inherited CPO, our simulations predict a strong *c*-axis maximum almost perpendicular to the shear plane under simple shear boundary conditions (series A and B). In both series, the *a*-axes reorient following the elongation axis of the new regime (*i.e.*, long axis of the finite-strain ellipsoid, FSE) with high-strain rate domains oriented parallel to the shear plane (see high-strain orientations in series A and B in Fig. 7). Following these results, the CPO developed in ice accumulated in a dome or a ridge would be overprinted at depth by the dominance of shearing parallel to the bedrock. Considering strain rates as at modelled the base of the EDML ($\sim 9\times10^{-11}\text{s}^{-1}$ ; Weikusat et al., 2017) the CPO would be preserved for a most of $\sim 2{,}8$ kyr. These predicted CPOs are in accordance with the observations of CPO analyses from most deep ice drill cores located on sites with the ice frozen to the bed in Antarctica and

Greenland, where an approximately vertical single maximum CPO is found (*e.g.*, Faria et al.,
2014; Montagnat et al., 2014a; Weikusat et al., 2017).

Simulations predict that the land-based ice CPO is destroyed at the ice shelf, assuming the example of shearing in the horizontal plane (*xy*) as the dominant deformation regime, as observed in the Antarctic Amery (Young et al., 2002) or Western Ross ice shelfs (LeDoux et al., 2017; Lutz et al., 2020). In this case, although the inherited vertical girdle CPO is not completely destroyed at the end of the simulation, it is progressively overprinted by the shearing in the horizontal plane, (series D in Fig. 7).  Assuming strain rates calculated in ice shelves ($\sim 5\mathrm{x}10^{-11}\mathrm{s}^{-1}$ ; Millstein et al., 2021) the inherited fabric would be preserved for at most $\sim 2,5$ kyr.

When an inherited single vertical maximum is affected by extension along the flow, similar to ice flowing in an ice stream that previously accumulated in an ice dome, the CPO is also progressively overprinted, but the required strain is clearly much higher than that for the other cases ($\varepsilon > 1.2$) (series C Fig. 7). Simulations predict that ice moving into a shear margin or potentially developing a shear margin during the initiation of an ice stream, will basically lose its original CPO as shearing in the horizontal plane (*xy*) overprints the inherited fabric. As observed in the simulations, the effectiveness of the second flow regime on the reorientation of the CPO depends not only on the strength of the inherited CPO, but also on the relationship between the crystal orientation and the finite-strain ellipsoid of the new imposed regime. When the maximum elongation axis of the new finite-strain ellipsoid lies within the inherited *a*-axis girdle (see series C and D in Fig. 7) *c*-axis orientations are more slowly modified. This is in accordance with our understanding of dislocation motion, because the most efficient dislocations in ice (basal dislocations) do have a Burgers vector component (glide direction) along the *a*-axes.

The flow behaviour from the pole figure observed in Series C at $\varepsilon_1 = 1.2$ and $\varepsilon_2 = 1.2$ (see lower right corner in Fig. 5a) could easily be misinterpreted as axial compression in the *z*-direction (Fig. 3b), while the true current flow is axial extension in the *x*-direction. The effectivity of the second flow regime is also observable in the relative activity of slip systems (Fig.8). In all cases, the new imposed regime produces a remarkable increment of basal slip, while the pyramidal slip system activity is reduced (see series A, B and D in Fig.8). A different effect is found when an inherited vertical single maximum is affected by extension along the flow direction, where the basal activity remains constant, and the prismatic slip is increased (see series C in Fig.8).
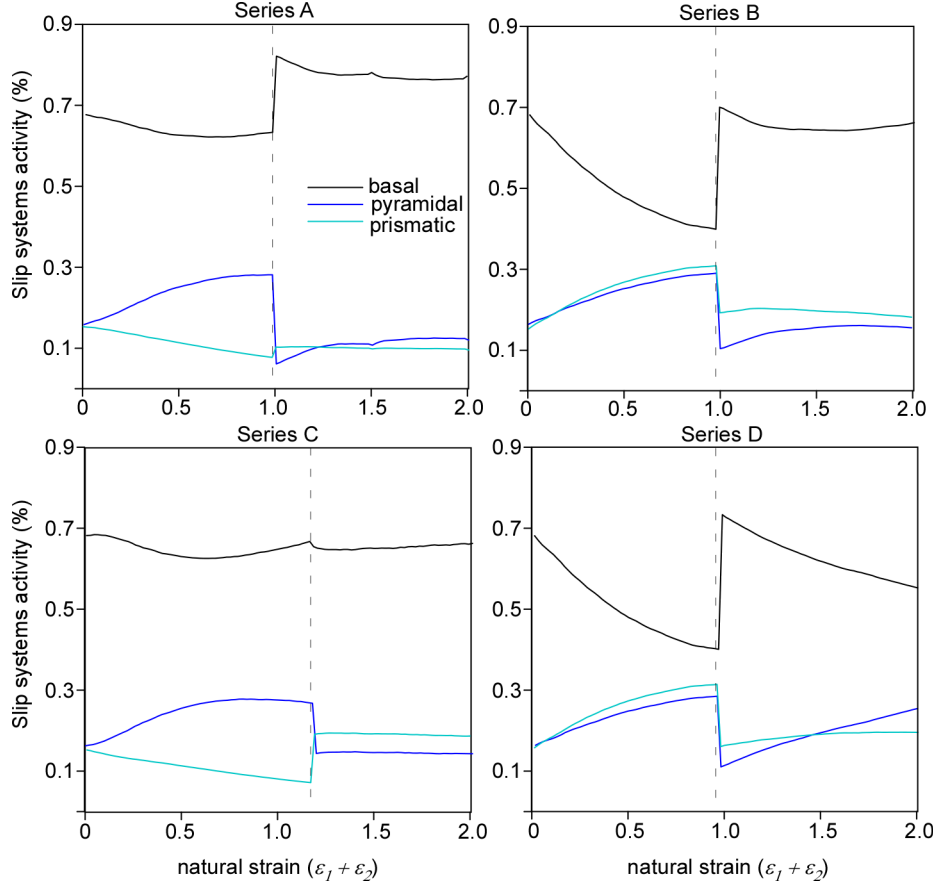
**Figure 8.** Evolution of the relative activities of basal, pyramidal and prismatic slip systems during deformation for all series presented, calculated from Equation (1). Transition of deformation regimes are marked with a vertical dashed line. In A, B and D series, the second flow regime produces a remarkable increment of basal slip, while the pyramidal slip system activity is reduced. However, in series C the basal activity remains constant, and the prismatic slip is increased.

All these results demonstrate that an inherited CPO can change entirely within strains of $\varepsilon$ <1.2 with a range of transition fabrics (Fig.9). Our results suggest that, under natural conditions, as for example those at the onset of the NEGIS, where the velocity increases by 40 m/yr over a distance of 120 km (i.e., strain rate of ~1x10$^{-11}$ s$^{-1}$) (Joughin et al., 2018) an inherited fabric would be preserved for at most ~ 7 kyr. However, in the NEGIS margins, where the flow is considerably faster (i.e., strain rate of ~ 4x10$^{-10}$ s$^{-1}$) (Joughin et al., 2018), an inherited fabric would be destroyed in a mere ~ 200 years. This process depends on both the intensity of the inherited CPO, and its orientation with respect to the new flow regime. These results are in agreement with ice experiments of natural samples with a pre-existing CPO, where the application of a stress field in a non-favourable orientation with respect to the inherited CPO destroys it (Jun and Jacka, 1998, Craw et al., 2018).

One particular case is an inherited strong CPO, where *a*-axes are optimally oriented with

respect to the second flow regime, because the finite-strain ellipsoid elongation axis from the first and second regime are in the same plane (see FSA in series C and D in Fig.8). In this situation the second regime does not produce a rapid re-orientation of the *a*-axes with respect to the elongation axis, the basal activity is not enhanced and therefore the CPO is slowly modified (series C and D in Fig.9). In this case the required finite strain for overprinting the initial CPO is clearly much higher than that for the other cases.

The entire change of a previous CPO also takes place in other rocks, such as olivine-rich rocks in the upper mantle, where a new CPO quickly develops according to the new imposed boundary conditions. The observed CPO will thus not record the full history of changes in the kinematics of deformation (Kaminski, 2004). However, as our results reveal, the re-orientation of an inherited CPO depends both on its intensity and on the orientation with respect to the new stress field. These results are in agreement with observations from olivine experiments, where the pre-existing texture orientation determines the way the texture evolves (Boneh and Skemer, 2014). Accordingly, the deformation history could have an impact on the CPO in areas with complex flow, as in subduction zones (Di Leo et al., 2014; Li et al., 2014).
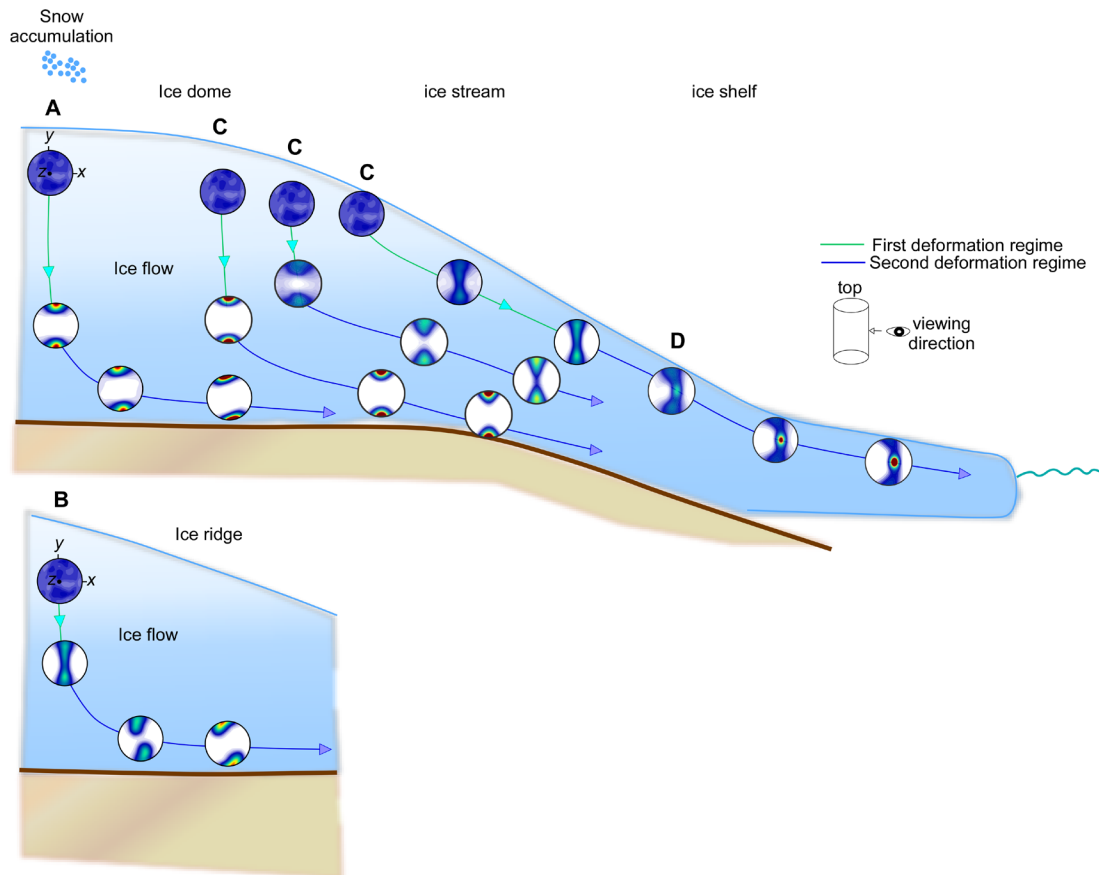
**Figure 9.** Prediction of evolution of *c*-axis (0001) orientation in all series presented (from A to D), according to the deformation conditions assumed in figure 1. A flow change produces an overprint of the previous CPO, with

525     a range of transition fabrics.

**6. Model limitations**

530     A number of studies that used the VPFFT-ELLE modelling approach (e.g., in Llorens et al.,
        2016a, 2016b and 2017; Steinbach et al., 2017 and Gomez-Rivas et al., 2017) have shown
        that dynamic recrystallisation processes, including grain boundary migration, recovery and
        polygonization, have a minor effect on the CPO development (orientation and strength). The
        implementation of DRX in our models does not change the time scale during the
535     development of a preferred crystallographic orientation, as shown in supplementary figure 4,
        where series with and without DRX are compared. However, this may depend on the
        particular recrystallisation process, for example, (1) spontaneous nucleation (i.e., nucleation
        of new, strain-free grains), or (2) rotation of small grains due to grain boundary sliding. In the
        first case the microstructure would be influenced by the orientation of these new crystals
540     (Thorsteinsson et al., 2003), weakening the CPO. As shown in experiments (Fan et al., 2020)
        activation of grain boundary sliding in the small grains also reduces the CPO strength. It
        however remains unclear to which extent these two recrystallisation processes play a role in
        the natural deformation of ice

545     **7. Conclusions**

        This study presents a series of full-field numerical simulations of non-linear viscous
        polycrystalline ice deformed under two consecutive flow regimes. The analysis of the
        resulting crystallographic preferred orientation (CPO) leads to the following main
550     conclusions:
        1. Simulations with an initial random distribution of crystallographic orientations predict a
        quick alignment ($\varepsilon$< 0.4) of the crystallographic axes according to the imposed boundary
        conditions. In all cases, ice polycrystals develop a CPO with $c$-axes mostly oriented parallel
        to the compression axis, and $a$-axes oriented parallel to the elongation axis of the finite strain
555     ellipsoid.
        2. Depending on the sequence of deformation regimes, an inherited CPO can be completely
        overprinted by the later deformation event. An inherited CPO can change entirely within a
        natural strain lower than 1.2, with a range of transitional fabrics. This process depends both

on the intensity of the inherited CPO and its orientation with respect to the new stress field.

3. More specifically, when the inherited *a*-axis preferred orientation and the elongation axis of the finite strain ellipse of the flow are parallel, lattice orientation only needs to be reoriented slightly. The required finite strain for overprinting the initial CPO in this configuration is much higher ($\varepsilon$>1.2) than that for the other cases. This is the case of ice flowing from an ice dome to an ice stream. This situation could lead to a misinterpretation of the second flow regime from the observed *c*-axis preferred orientation.

4. According to our results, CPOs are reliable indicators of the current flow conditions, as they usually adapt to them in a relatively short time. However, caution is warranted when a volume of ice may have experienced complex (multi-stage) deformation histories.

## Acknowledgements

MGL acknowledges a Juan de la Cierva-Incorporación fellowship (IJC2018-036826-I), funded by the MCIN/AEI/10.13039/501100011033. EGR acknowledges the support of the Ramón y Cajal fellowship (RYC2018-026335-I), funded by the MCIN/AEI/10.13039/501100011033 and the FSE. IW acknowledges the HFG grant no.VH-NG-802. This work is part of the CSIC-PTI POLARCSIC activities, and it has been developed using the facilities of the Laboratory of Geodynamic Modelling of GEO3BCN and a computer cluster of the University of Tübingen.

## References

Alley, R.B. Fabrics in polar ice sheets: development and prediction. Science, 240, 493-495. 1988

Azuma, N. and Higashi, A. Mechanical properties of dye 3 Greenland deep ice cores. Annals of glaciology, 5 ,1-8. 1984

Azuma, N., Wang, Y., Mori, K., Narita, H., Hondoh, T., Shoji and H.,Watanabe, O. Textures and fabrics in the Dome F (Antarctica) ice core. *Annals of Glaciology*, *29*, pp.163-168. 1999

Bachmann, F., Hielscher, R. and Schaeben, H. Grain detection from 2d and 3d EBSD data— Specification of the MTEX algorithm. *Ultramicroscopy*, *111*(12), pp.1720-1733. 2011

Boneh, Y. and Skemer, P. The effect of deformation history on the evolution of olivine CPO. *Earth and Planetary Science Letters*, *406*, pp.213-222. 2014

Bons, P.D., Koehn, D. and Jessell, M.W. Microdynamic Simulation. Lecture Notes in Earth Sciences 106, Springer, Berlin. 405 pp. 2008

595 Bons, P.D., Kleiner, T., Llorens, M.G., Prior, D.J., Sachau, T., Weikusat, I. and Jansen, D. Greenland Ice Sheet: Higher nonlinearity of ice flow significantly reduces estimated basal motion. Geophysical Research Letters, 45(13), pp.6542-6548. 2018.

Budd, W. and Jacka, T. A review of ice rheology for ice sheet modelling. Cold Regions Sci. Technol., 16(2), 107–144. doi: 10.1016/0165-232X(89)90014-1. 1989.

600 Budd, W.F., Warner, R.C., Jacka, T.H., Li, J., Treverrow, A. Ice flow relations for stress and strain-rate components from combined shear and compression laboratory experiments. J. Glaciol. 59, 374–392. 2013.

Castelnau, O., Shoji, H., Mangeney, A., Milsch, H., Duval, P., Miyamoto, A., Kawada and K.,Watanabe, O. Anisotropic behavior of GRIP ices and flow in central Greenland. 605 Earth and planetary science letters, 154(1-4), pp.307-322. 1998

Craw, L., Qi, C., Prior, D.J., Goldsby, D.L. and Kim, D. Mechanics and microstructure of deformed natural anisotropic ice. J. Struct. Geol. 115, 152–166. 2018

Dahl‑Jensen, D., Thorsteinsson, T., Alley, R. and Shoji, H. Flow properties of the ice from the Greenland Ice Core Project ice core: the reason for folds?. Journal of Geophysical 610 Research: Oceans, 102(C12), pp.26831-26840. 1997

Di Leo, J.F., Walker, A.M., Li, Z.H., Wookey, J., Ribe, N.M., Kendall, J.M. and Tommasi, A. Development of texture and seismic anisotropy during the onset of subduction. *Geochemistry, Geophysics, Geosystems*, *15*(1), pp.192-212. 2014

Durand, G., Gillet-Chaulet, F., Svensson, A., Gagliardini, O., Kipfstuhl, S., Meyssonnier, J., 615 Parrenin, F., Duval, P. and Dahl-Jensen, D. Change in ice rheology during climate variations–implications for ice flow modelling and dating of the EPICA Dome C core. *Climate of the Past*, *3*(1), pp.155-167. 2007

Duval, P., Ashby, M.F. and Anderman, I. Rate-controlling processes in the creep of polycrystalline ice. The Journal of Physical Chemistry, 87(21), pp.4066-4074. 1983

620 Edwards, T.L., Nowicki, S., Marzeion, B., Hock, R., Goelzer, H., Seroussi, H., Jourdain, N.C., Slater, D.A., Turner, F.E., Smith, C.J. and McKenna, C.M. Projected land ice contributions to twenty-first-century sea level rise. *Nature*, *593*(7857), pp.74-82. 2021.

Fan, S., Hager, T.F., Prior, D.J., Cross, A.J., Goldsby, D.L., Qi, C., Negrini and Wheeler, J. Temperature and strain controls on ice deformation mechanisms: insights from the microstructures of samples deformed to progressively higher strains at− 10,− 20 and− 30° C. The Cryosphere, 14(11), pp.3875-3905. 2020

Faria, S. H., Weikusat, I., and Azuma, N. The microstructure of polar ice. Part I: Highlights from ice core research, J. Struct. Geol., 61, 2–20 https://doi.org/10.1016/j.jsg.2013.09.010, 2014

Golledge, N. R., Kowalewski, D. E., Naish, T. R., Levy, R. H., Fogwill, C. J. and Gasson, E. G. W. The multi-millennial Antarctic commitment to future sea-level rise, Nature, 526, 421–425, https://doi.org/10.1038/nature15706. 2015.

Griera, A., Llorens, M.G., Gomez-Rivas, E., Bons, P.D., Jessell, M.W., Evans, L.A. and Lebensohn, R.. Numerical modelling of porphyroclast and porphyroblast rotation in anisotropic rocks. Tectonophysics, 587, pp.4-29. 2013.

Gomez‐Rivas, E., Griera, A., Llorens, M.G., Bons, P.D., Lebensohn, R.A. and Piazolo, S. Subgrain rotation recrystallization during shearing: insights from full‐field numerical simulations of halite polycrystals. Journal of Geophysical Research: Solid Earth, 122(11), pp.8810-8827. 2017

Gow, A.J., Meese, D.A., Alley, R.B., Fitzpatrick, J.J., Anandakrishnan, S., Woods, G.A. and Elder, B.C. Physical and structural properties of the Greenland Ice Sheet Project 2 ice core: A review. *Journal of Geophysical Research: Oceans*, *102*(C12), pp.26559-26575. 1997

Haefeli, R. Contribution to the movement and the form of ice sheets in the Arctic and Antarctic. Journal of Glaciology, 3(30), pp.1133-1151. 1961

Hudleston, P.J. Structures and fabrics in glacial ice: a review. Journal of Structural Geology, 81, pp.1-27. 2015

Jacka, T.H. and Maccagnan, M. Ice crystallographic and strain rate changes with strain in compression and extension. *Cold Regions Science and Technology*, *8*(3), pp.269-286. 1984

Jacka, T.H. and Li, J. Flow rates and crystal orientation fabrics in compression of polycrystalline ice at low temperatures and stresses. In Hondoh T ed. *Physics of ice core records*. Hokkaido University Press, Sapporo, 83–102. 2000

Jansen, D., Llorens, M.G., Westhoff, J., Steinbach, F., Kipfstuhl, S., Bons, P.D., Griera, A. and Weikusat, I. Small-scale disturbances in the stratigraphy of the NEEM ice core:

observations and numerical model simulations. The Cryosphere, 10(1), pp.359-370. 2016

Jennings, S. J. A., & Hambrey, M. J. Structures and deformation in glaciers and ice sheets. *Reviews of Geophysics*, 59, e2021RG000743. 2021. https://doi.org/10.1029/2021RG000743

Joughin, I.A.N., Smith, B.E. and Howat, I.M. A complete map of Greenland ice velocity derived from satellite data collected over 20 years. Journal of Glaciology, 64(243), pp.1-11. 2018

Jun, L. and Jacka, T.H. Horizontal shear rate of ice initially exhibiting vertical compression fabrics. Journal of Glaciology, 44(148), pp.670-672. 1998

Kamb, B., 1972. In: Experimental Recrystallization of Ice under Stress. Flow and Fracture of Rocks, vol. 16. American Geophysical Union Geophysical Monograph, pp. 211–241 California I. of T.

Kaminski, E., Ribe, N.M. and Browaeys, J.T. D-Rex, a program for calculation of seismic anisotropy due to crystal lattice preferred orientation in the convective upper mantle. Geophysical Journal International, 158(2), pp.744-752. 2004

Katayama, I. and Karato, S.I. Effect of temperature on the B-to C-type olivine fabric transition and implication for flow pattern in subduction zones. Physics of the Earth and Planetary Interiors, 157(1-2), pp.33-45. 2006

Kim, D., Prior, D.J., Han, Y., Qi, C., Han, H. and Ju, H.T. Microstructures and Fabric Transitions of Natural Ice from the Styx Glacier, Northern Victoria Land, Antarctica. Minerals, 10(10), p.892. 2020

Lebensohn, R.A. and Rollett, A.D. Spectral methods for full-field micromechanical modelling of polycrystalline materials. Computational Materials Science, 173, p.109336. 2020

Li, Z.H., Di Leo, J.F. and Ribe, N.M. Subduction‐induced mantle flow, finite strain, and seismic anisotropy: Numerical modeling. Journal of Geophysical Research: Solid Earth, 119(6), pp.5052-5076. 2014

Llorens, M. G., Griera, A., Bons, P. D., Roessiger, J., Lebensohn, R., Evans, L. and Weikusat, I. Dynamic recrystallisation of ice aggregates during co-axial viscoplastic deformation: a numerical approach. Journal of Glaciology 62, 359-377. 2016a

Llorens, M. G., Griera, A., Bons, P. D., Lebensohn, R. A., Evans, L. A., Jansen, D. and Weikusat, I. Full field predictions of ice dynamic recrystallisation under simple shear conditions. Earth and Planetary science letters 450, 233-242. 2016b

690 Llorens, M.G., Griera, A., Steinbach, F., Bons, P.D., Gomez-Rivas, E., Jansen, D., Roessiger, J., Lebensohn, R.A. and Weikusat, I. Dynamic recrystallization during deformation of polycrystalline ice: insights from numerical simulations. *Philosophical Transactions of the Royal Society A: Mathematical, Physical and Engineering Sciences*, *375*(2086), p.20150346. 2017

695 Llorens, M.G., Griera, A., Bons, P.D., Gomez-Rivas, E., Weikusat, I., Prior, D.J., Kerch, J. and Lebensohn, R.A. Seismic anisotropy of temperate ice in polar ice sheets. *Journal of Geophysical Research: Earth Surface*, *125*(11), p.e2020JF005714. 2020

LeDoux, C.M., Hulbe, C.L., Forbes, M.P., Scambos, T.A. and Alley, K. Structural provinces of the ross ice shelf, antarctica. Annals of Glaciology, 58(75pt1), pp.88-98. 2017

700 Lilien, D.A., Rathmann, N.M., Hvidberg, C.S. and Dahl‐Jensen, D. Modeling Ice‐Crystal Fabric as a Proxy for Ice‐Stream Stability. Journal of Geophysical Research: Earth Surface, 126(9), p.e2021JF006306. 2021

Lipenkov, V.Y., Barkov, N.I., Duval, P. and Pimienta, P. Crystalline Texture of the 2083 m Ice Core at Vostok Station, Antarctica. J. Glaciol., 35, 392–398. 1989

705 Lutz, F., Eccles, J., Prior, D.J., Craw, L., Fan, S., Hulbe, C., Forbes, M., Still, H., Pyne, A. and Mandeno, D. Constraining Ice Shelf Anisotropy Using Shear Wave Splitting Measurements from Active-Source Borehole Seismics. Journal of Geophysical Research: Earth Surface, 125(9), p.e2020JF005707. 2020

Millstein, J., Minchew, B. and Pegler, S.S. Reassessing the flow law of glacier ice using
710 satellite observations. https://doi.org/10.31223/X5D32X. 2021

Montagnat, M., Blackford, J.R., Piazolo, S., Arnaud, L. and Lebensohn, R.A. Measurements and full-field predictions of deformation heterogeneities in ice. Earth Planet. Sci. Lett., 305(1–2), 153– 160 (doi: 10.1016/j.epsl.2011.02.050). 2011.

Montagnat, M., Buiron, D., Arnaud, L., Broquet, A., Schlitz, P., Jacob, R. and Kipfstuhl, S.
715 Measurements and numerical simulation of fabric evolution along the Talos Dome ice core, Antarctica. *Earth and Planetary Science Letters*, *357*, pp.168-178. 2012

Montagnat, M., Azuma, N., Dahl-Jensen, D., Eichler, J., Fujita, S., Gillet-Chaulet, F., Kipfstuhl, S., Samyn, D., Svensson, A. and Weikusat, I. Fabric along the NEEM ice core, Greenland, and its comparison with GRIP and NGRIP ice cores. 2014a

720  Montagnat, M., Castelnau, O., Bons, P.D., Faria, S.H., Gagliardini, O., Gillet-Chaulet, F.,
       Grennerat, F., Griera, A., Lebensohn, R.A., Moulinec, H., Roessiger, J. and Suquet, P.
       Multiscale modeling of ice deformation behavior. Journal of Structural Geology 61, 78-
       108. dx.doi.org/10.1016/j.jsg.2013.05.002. 2014b

Nerem, R.S., Beckley, B.D., Fasullo, J.T., Hamlington, B.D., Masters, D. and Mitchum, G.T.
725    Climate-change–driven accelerated sea-level rise detected in the altimeter era.
       Proceedings of the national academy of sciences, 115(9), pp.2022-2025. 2018

Passchier, C.W. Reconstruction of deformation and flow parameters from deformed vein sets.
       Tectonophysics 180, 185- 199. 1990.

Peternell, M. and Wilson, C.J. Effect of strain rate cycling on microstructures and
730    crystallographic preferred orientation during high-temperature creep. Geology, 44(4),
       pp.279-282. 2016

Piazolo, S., Bons, P.D., Griera, A., Llorens, M.G., Gomez-Rivas, E., Koehn, D., Wheeler, J.,
       Gardner, R., Godinho, J.R., Evans, L. and Lebensohn, R.A. A review of numerical
       modelling of the dynamics of microstructural development in rocks and ice: Past,
735    present and future. Journal of Structural Geology, 125, pp.111-123. 2019

Qi, C., Prior, D.J., Craw, L., Fan, S., Llorens, M.G., Griera, A., Negrini, M., Bons, P.D. and
       Goldsby, D.L. Crystallographic preferred orientations of ice deformed in direct-shear
       experiments at low temperatures. The Cryosphere, 13(1), pp.351-371. 2019

Skemer, P., Katayama, I., Jiang, Z. and Karato, S.I. The misorientation index: Development
740    of a new method for calculating the strength of lattice-preferred orientation.
       Tectonophysics, 411(1-4), pp.157-167. 2005

Steinbach, F., Bons, P.D., Griera, A., Jansen, D., Llorens, M.G., Roessiger, J. and Weikusat,
       I. Strain localization and dynamic recrystallization in the ice–air aggregate: a numerical
       study. The Cryosphere, 10(6), pp.3071-3089. 2016

745  Thorsteinsson, T., Kipfstuhl, J. and Miller, H. Textures and fabrics in the GRIP ice core. J.
       Geophys. Res. Ocean. 102, 26583–26599. 1997

Thorsteinsson, T., Waddington, E.D. and Fletcher, R.C. Spatial and temporal scales of
       anisotropic effects in ice-sheet flow. *Annals of Glaciology*, *37*, pp.40-48. 2003

Treverrow, A., Budd, W.F., Jacka, T.H. amd Warner R.C. The tertiary creep of
750    polycrystalline ice: experimental evidence for stress dependent levels of strain rate
       enhancement. J. Glaciol., 58 (208), 301–314. doi: 10.3189/2012JoG11J149. 2012

Vaughan, M.J., Prior, D.J., Jefferd, M., Brantut, N., Mitchell, T.M. and Seidemann, M.
       Insights into anisotropy development and weakening of ice from in situ P wave velocity

monitoring during laboratory creep. Journal of Geophysical Research: Solid Earth, 122(9), pp.7076-7089. 2017

Voigt, D.E. c-Axis Fabric of the South Pole Ice Core, SPC14. U.S. Antarctic Program (USAP) Data Center. doi: https://doi.org/10.15784/601057. 2017

Vollmer, F.W. An application of eigenvalue methods to structural domain analysis. Geological Society of America Bulletin, 102(6), pp.786-791.1990

Young, N.W. and Hyland, G. Velocity and strain rates derived from InSAR analysis over the Amery Ice Shelf, East Antarctica. Annals of Glaciology, 34, pp.228-234. 2002

Wang, Y., Thorsteinsson, T., Kipfstuhl, J., Miller, H., Dahl-Jensen, D. and Shoji, H. A Vostok-type fabric in the NGRIP deep ice core, North Greenland. Ann. Glaciol. 2002

Weikusat, I., Jansen, D., Binder, T., Eichler, J., Faria, S.H., Wilhelms, F., Kipfstuhl, S., Sheldon, S., Miller, H., Dahl-Jensen and D., Kleiner, T. Physical analysis of an Antarctic ice core—towards an integration of micro-and macrodynamics of polar ice. Philosophical Transactions of the Royal Society A, 375(2086), p.20150347. 2017

Wilson, C.J.L. Fabrics in polycrystalline ice deformed experimentally at –108C. *Cold* Reg. Sci. Technol., **6**(2), 149–161. 1982.

Wilson, C.J., Peternell, M., Hunter, N.J. and Luzin, V. Deformation of polycrystalline D2O ice: Its sensitivity to temperature and strain-rate as an analogue for terrestrial ice. Earth and Planetary Science Letters, 532, p.115999. 2020

Wilson, C.J.L., Peternell, M.A. Ice deformed in compression and simple shear: control of temperature and initial fabric. *Journal of Glaciology* 58, 11-22. 2012.